

UC Berkeley

UC Berkeley Previously Published Works

Title

Glial swip-10 controls systemic mitochondrial function, oxidative stress, and neuronal viability via copper ion homeostasis.

Permalink

<https://escholarship.org/uc/item/0n39c2h0>

Journal

Proceedings of the National Academy of Sciences of the United States of America, 121(39)

Authors

Rodriguez, Peter

Kalia, Vrinda

Fenollar-Ferrer, Cristina

et al.

Publication Date

2024-09-24

DOI

10.1073/pnas.2320611121

Peer reviewed



Glial *swip-10* controls systemic mitochondrial function, oxidative stress, and neuronal viability via copper ion homeostasis

Peter Rodriguez^a, Vrinda Kalia^b, Cristina Fenollar-Ferrer^{c,d}, Chelsea L. Gibson^{a,e}, Zayna Gichif, Andre Rajoo^e, Carson D. Matier^{h,i}, Aidan T. Pezacki^{h,i,j}, Tong Xiao^{h,i,j}, Lucia Carvelli^{d,f,g}, Christopher J. Chang^{h,i,j}, Gary W. Miller^b, Andy V. Khamoui^{d,k}, Jana Boerner^d, and Randy D. Blakely^{d,f,1}

Affiliations are included on p. 11.

Edited by Monica Driscoll, Rutgers The State University of New Jersey, Piscataway, NJ; received December 11, 2023; accepted August 1, 2024

Cuprous copper [Cu(I)] is an essential cofactor for enzymes that support many fundamental cellular functions including mitochondrial respiration and suppression of oxidative stress. Neurons are particularly reliant on mitochondrial production of ATP, with many neurodegenerative diseases, including Parkinson's disease, associated with diminished mitochondrial function. The gene *MBLAC1* encodes a ribonuclease that targets pre-mRNA of replication-dependent histones, proteins recently found in yeast to reduce Cu(II) to Cu(I), and when mutated disrupt ATP production, elevates oxidative stress, and severely impacts cell growth. Whether this process supports neuronal and/or systemic physiology in higher eukaryotes is unknown. Previously, we identified *swip-10*, the putative *Caenorhabditis elegans* ortholog of *MBLAC1*, establishing a role for glial *swip-10* in limiting dopamine (DA) neuron excitability and sustaining DA neuron viability. Here, we provide evidence from computational modeling that SWIP-10 protein structure mirrors that of *MBLAC1* and locates a loss of function coding mutation at a site expected to disrupt histone RNA hydrolysis. Moreover, we find through genetic, biochemical, and pharmacological studies that deletion of *swip-10* in worms negatively impacts systemic Cu(I) levels, leading to deficits in mitochondrial respiration and ATP production, increased oxidative stress, and neurodegeneration. These phenotypes can be offset in *swip-10* mutants by the Cu(I) enhancing molecule elesclomol and through glial expression of wildtype *swip-10*. Together, these studies reveal a glial-expressed pathway that supports systemic mitochondrial function and neuronal health via regulation of Cu(I) homeostasis, a mechanism that may lend itself to therapeutic strategies to treat devastating neurodegenerative diseases.

C. elegans | *swip-10* | glia | copper | neurodegeneration

Copper (Cu) is an essential micronutrient involved in numerous fundamental aspects of cell physiology including mitochondrial respiration, ATP production, suppression of oxidative stress, redox-dependent biosynthetic pathways, and metal ion-supported cell signaling (1–3). The ability of Cu to readily accept and donate electrons is essential to the activities of Cu-dependent proteins (4). Among the most well-studied roles for Cu are the detoxification of reactive oxygen species (ROS) and support for mitochondrial electron transport chain (ETC) function, provided by Cu-dependent superoxide dismutase (SOD) and cytochrome c oxidase (CytC), respectively (5). In turn, mitochondrial function, and ROS buffering are key determinants of neuronal health and signaling (6). Indeed, a large amount of dietary Cu ultimately is stored and used in the brain (~6%), second only to the liver and muscle in Cu concentrations (7). Menke's disease and Wilson's disease, genetic disorders characterized by systemic diminished and excess Cu concentrations, respectively, result in neurodegeneration (8). Altered CNS Cu homeostasis has also been linked to more common neurodegenerative diseases (NDDs), including Alzheimer's disease (AD) and Parkinson's disease (PD) (8). Cu exists in biological systems primarily in one of two ionic forms, cuprous Cu [Cu(I)] and cupric Cu [Cu(II)]. Cu(I) and Cu(II) are handled by different chaperones and transporters (5), and the interconversion between the two supports a host of enzymatic reactions. How a proper balance of these Cu forms is achieved continues to be an active area of investigation. Recent studies using the *Saccharomyces cerevisiae* model revealed an essential role of histone H3:H4 complexes in Cu-dependent mitochondrial function, suppression of oxidative stress, and cell growth. Specifically, H3:H4 histone complexes were found to possess Cu(II) reductase activity, a function independent of the role of these proteins in nucleosome formation and gene regulation (9). In this model, histone Cu reductase function is quantitatively critical with respect to the provision of Cu(I) for mitochondrial electron transport by cytochrome C oxidase

Significance

Energetic deficiencies contribute to multiple neurodegenerative diseases, including Alzheimer's and Parkinson's disease. Cuprous Cu [Cu(I)] is a vital micronutrient, playing a critical role in ATP production and in limiting oxidative stress. We demonstrate that glial expression of the *Caenorhabditis elegans* gene *swip-10* plays an essential role in systemic Cu(I) homeostasis and its metabolic consequences. Whereas loss of *swip-10* drives body-wide reductions in mitochondrial function and ATP production, elevates oxidative stress, and induces dopamine neuron degeneration, treatments that elevate Cu(I), or restore *swip-10* expression in glia, significantly limit these changes. Our work implicates *swip-10* and orthologs as key determinants of Cu(I) homeostasis that may be exploitable to treat neurodegenerative diseases and their metabolic comorbidities.

Author contributions: P.R., C.F.-F., C.L.G., G.W.M., and R.D.B. designed research; P.R., V.K., C.F.-F., C.L.G., Z.G., A.R., T.X., and J.B. performed research; C.D.M., A.T.P., C.J.C., G.W.M., and A.V.K. contributed new reagents/analytic tools; P.R., V.K., C.F.-F., C.L.G., L.C., G.W.M., A.V.K., and R.D.B. analyzed data; and P.R., C.F.-F., and R.D.B. wrote the paper.

The authors declare no competing interest.

This article is a PNAS Direct Submission.

Copyright © 2024 the Author(s). Published by PNAS. This article is distributed under Creative Commons Attribution-NonCommercial-NoDerivatives License 4.0 (CC BY-NC-ND).

¹To whom correspondence may be addressed. Email: rblakely@health.fau.edu.

This article contains supporting information online at <https://www.pnas.org/lookup/suppl/doi:10.1073/pnas.232061121/-/DCSupplemental>.

Published September 17, 2024.

(CytC) and reduction of oxidative stress by Cu-dependent superoxide dismutase (SOD) (5). Whether this pathway plays a role in multicellular organisms and for neuronal health and signaling has yet to be established, though the metabolic and growth defects of a yeast model of Friedreich's ataxia can be rescued through manipulation of H3 histone Cu reductase activity (10).

Our lab has utilized the genetic model system *Caenorhabditis elegans* to elucidate genetic pathways that support signaling and health of multiple classes of neurons including those secreting dopamine (DA) (11–16), the class of neurons that degenerate in PD (17). For example, we demonstrated that worms labeled through DA neuron-specific green fluorescent protein (GFP) expression are damaged, like mammalian DA neurons, by brief incubations with the neurotoxin 6-OHDA, effects prevented in animals lacking the gene encoding the presynaptic DA transporter (*dat-1*), a known mediator of DA neuron-specific uptake of the toxin. Subsequently, we found that *dat-1* deletion leads to rapid paralysis when mutant animals are placed in water (18), a phenotype termed Swimming Induced Paralysis (Swip). The robust and highly reproducible nature of the Swip phenotype and its reliance on DA signaling prompted us to adopt it for a forward genetic screen to identify molecular molecules required to support the function and health of DA neurons (19). Importantly, this screen identified multiple worm lines with mutations in *dat-1*, whose Swip phenotype could be reversed through pharmacological or genetic elimination of presynaptic DA stores and postsynaptic DA receptors (12, 19, 20).

In the course of our screens, we identified the previously unstudied gene *swip-10* and established that it acts cell nonautonomously via its expression in glial cells to limit DA signaling (19). Our functional studies revealed that loss of function *swip-10* mutants display Glu-dependent, DA neuron hyperexcitability that drives augmented DA release and produces Swip via excess activation of the motor neuron D2-type DA receptor DOP-3 (19, 20). Excess Glu signaling onto mammalian DA neurons results in DA neuron degeneration and has been proposed to be a contributor to PD (21, 22). Consistent with this hypothesis, our subsequent studies revealed a premature death of mutant *swip-10* DA neurons that could be attenuated by genetic elimination of Glu receptors (15). Interestingly, *swip-10* effects extended beyond DA neurons, as degeneration could also be observed in other neurons, specifically ones ensheathed by glia, whereas neurons lacking glial ensheathment appear unaffected. These findings reinforce a critical role of glia in supporting neuronal health and signaling (15) and Glu-dependent neurodegeneration that can arise from disrupted glial–neuron interactions (23). Last, we found elevations of whole-body oxidative stress, as visualized by the reporter *gst-4::GFP*, suggesting that, as seen with the systemic control of proteostasis (24, 25), glial cells play an important role in the worm in limiting body-wide ROS production.

Although *swip-10* mutants demonstrated readily discernable physiological, behavioral, and pathological changes, the normal function of SWIP-10 was unclear, owing to a lack of study, at that time, of related proteins. Amino acid sequence alignment of SWIP-10 to human proteins revealed strongest identity to the protein MBLAC1, driven by shared residues that comprise their Metallo β -lactamase Domains (MBD) (14). Conspicuously, although MBLAC1 had yet to be studied, both mutations recovered in our Swip screen were found to lie in the MBD, supporting a causal role for disruptions in the enzymatic function of this domain in *swip-10* phenotypes. Studies by Broce and colleagues (26) who associated a risk for AD with cardiovascular disease (CVD) comorbidity through genome-wide association studies and postmortem cortical *MBLAC1* mRNA expression studies, along

with the death of DA neurons in *swip-10* mutants, further encouraged our efforts to identify this activity. A potential clue to the function of the *swip-10* MBD arose from work of Pettinati and colleagues (27) who demonstrated that the MBLAC1 MBD encoded a 3' RNA endonuclease that targets pre-mRNA of replication dependent (RD), H3 histone proteins. Depletion of MBLAC1 in adenovirus-transformed kidney cells slowed cell cycle progression in vitro, in keeping a need for elevated RD histone expression to sustain mitosis. However, both *Mblac1*^{-/-} mice (28), as well as *swip-10* mutant worms, show no gross physical abnormalities, developmental defects, or lifespan alterations that would support a nonredundant contribution to cell cycle regulation in vivo. Moreover, RD histones are actively transcribed in postmitotic cells (29), including neurons (29, 30), and the most conspicuous phenotypes in *swip-10* mutants arise from the altered function and viability of postmitotic neurons.

Based on the Pettinati et al. findings demonstrating H3 histone RNA endonuclease activity and the Attar et al. studies revealing an unexpected Cu(II) reductase activity of H3:H4 histone complexes, we hypothesized that SWIP-10 might also contribute to Cu(I) production and homeostasis. Furthermore, we reasoned that without constraints for diffusion as with the mammalian blood–brain barrier, glia in the head might regulate cells in the periphery through this mechanism, demonstrable through a visualization of the major Cu(I) depot in the worm intestine (31). Here, we provide computational modeling findings that demonstrate highly significant 3D alignment of the predicted structure of SWIP-10 protein with crystalized MBLAC1, supporting a role for SWIP-10 in histone RNA processing. Moreover, through metabolic, biochemical, imaging, and genetic studies, we provide evidence that glial-expressed *swip-10* provides essential, systemic support for Cu(I) homeostasis and phenotypes dependent on the micronutrient's availability, including mitochondrial respiration, suppression of oxidative stress, and DA neuron viability.

Results

Structural Modeling-Based Analysis of Overlap of the SWIP-10 MBD with that of MBLAC1 Supports a Shared Role in RNA Processing.

The metallo β -lactamase (MBL) *gene* family harboring *swip-10* and *MBLAC1* shares a common fold (MBLf) that hydrolyzes a diverse array of substrates ranging from DNA and RNA to lipids and small organic molecules, and is composed of three genetically divergent subfamilies (Groups 1 to 3), with SWIP-10 and MBLAC1 proteins located in Group 1 (32). Group 1 substrates currently include RNA (MBLAC1, LACTB2), (S)-2-hydroxyacylglutathione thioester (HAGH) and glutathione persulfide (ETHE1), and acyl-CoA (MBLAC2). One member (PNKD) has yet to be deorphanized. In order to determine whether the 3D structure of the MBD of SWIP-10 has a similar fold to that of MBLAC1, as compared with other members of Group 1 and select members of Group 2, we utilized already available structures and AlphaFold (33) models, as described in *SI Appendix, Supplementary Methods*, and performed a structural superimposition of the corresponding MBDs using STAMP (34) (Fig. 1 and *SI Appendix, Figs. S1–S4*). The AlphaFold model superimposed on the crystal structure of MBLAC1 demonstrates an RMSD of 0.2, indicating high reliability of AlphaFold modeling of MBDs. Our analysis of the SWIP-10 AlphaFold model indicates that the residues within 10Å of the catalytic aspartate (Asp) that coordinates both metal ions and the nucleophilic water molecule (35) are distributed throughout five loops (1, 5) in SWIP-10 similar to the MBL of Group 1 (*SI Appendix, Fig. S1*). Loops 2, 3, and 5 in SWIP-10 contain four metal-binding motifs as described for MBLAC1 and other family members, whereas loop 4 in SWIP-10

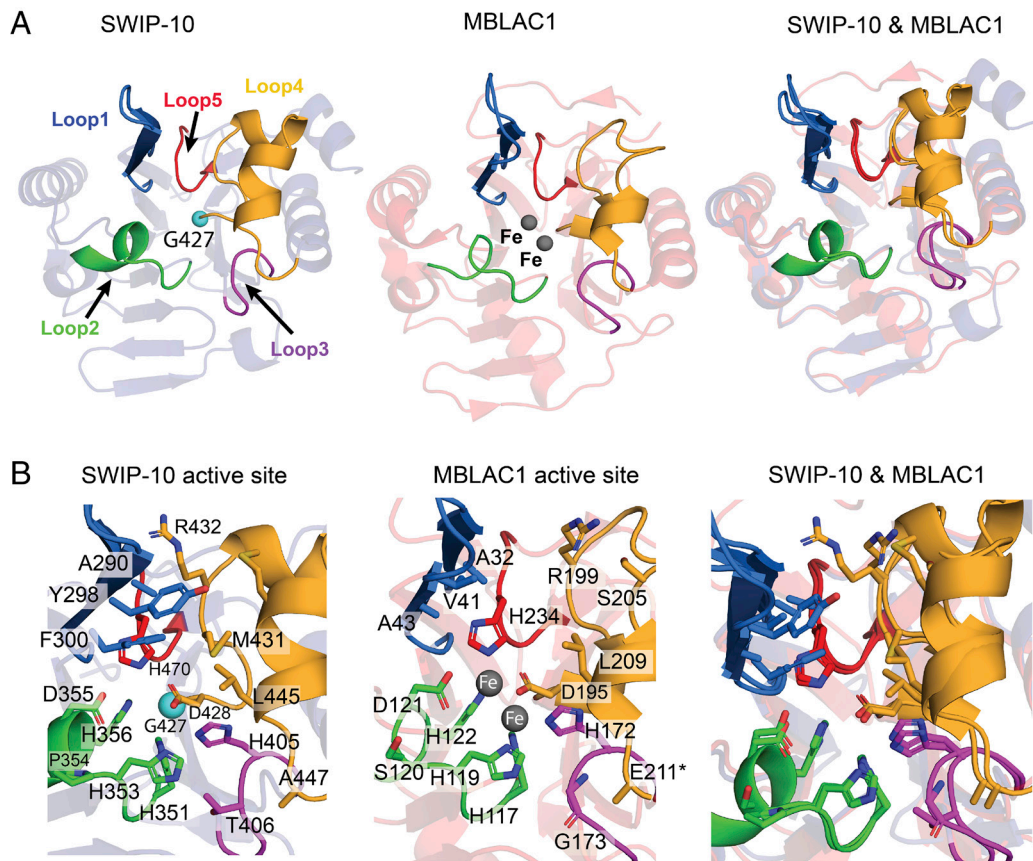


Fig. 1. Structural comparison of modeled SWIP-10 metallo b-lactamase domain (MBD) with the MBD of human MBLAC1. (A) Structural representation of the MBDS of crystallized human MBLAC1 [PDB id: 4V0H (27)] and modeled SWIP-10 obtained from the AlphaFold protein structure database, code: AF-Q20700-F1 (36) (Top view of the active sites). The percentage of residues of SWIP-10 and MBLAC1 overlapped after structural superimposition of both domains [using STAMP (34)] indicate that they share a similar fold (90% of residues in SWIP-10 MBD overlapped with homologous residues in MBLAC1). Loops surrounding the active site in both enzymes are colored in blue (Loop 1), green (Loop 2), magenta (Loop 3), orange (Loop 4), and red (Loop 5). Loop color is maintained in *SI Appendix, Supplemental Figures*. (B) Close view of the active site of both domains before and after their structural superimposition. Side chains located within 10Å of the catalytic Asp residue (D428 in SWIP-10 and 195 in MBLAC1) are shown as sticks and colored according to the loop in which are located. The presence of two Fe ions in the active site of the solved structure of MBLAC1, instead of the preferred Zn, are attributed by the authors to the expression system used for expression (*E. coli* instead of human cells) (27). A cyan sphere designates the C- α atom of G427 in MBLAC1 and is the site of a G427D mutation found in the *swip-10* mutant line vt33 (14). Residue numbering for MBLAC1 derives from the numbering used for the X-ray structure (27).

presents a similar length within members of Group1. Loop1 in SWIP-10 shares a similar length to those MBLs known to hydrolyze RNA, independently of the group to which they belong. This is not the case for MBLs of (HAGH, ETHE1, and PNKD), the first two as noted involved with glutathione-based detoxification reactions, as these MBDS have an extremely short loop 1 as well as other deviations. Finally, our SWIP-10 model positions a loss of function coding variant identified in our initial screen (14, 19) that lies immediately adjacent to an Asp residue whose position and orientation directly mirror an Asp of MBLAC1 that mutagenesis studies indicate is essential for RNA hydrolysis (35). Our STAMP analysis indicates that the MBD fold of SWIP-10 shares the highest similarity with that of MBLAC1 among all structures evaluated (*SI Appendix, Figs. S1–S4*) with 90% of the residues in these domains superimposed on the other. Similarly, the 3D disposition of the side chains of the conserved residues in loops 1 to 5 in SWIP-10 compared with MBLAC1 has an RMSD lower than 0.5 Å. Finally, their overall Structural Similarity Score of 7.48 indicates that the MBDS of SWIP-10 and MBLAC1 not only share a similar fold but is highly supportive of a similar function, ascribed to proteins with scores between 5.5 and 9.8 (*SI Appendix, Table S1*) (34).

Systemic Cu(I) Homeostasis is Supported by Expression of *swip-10*. With the similarities evident between SWIP-10 and MBLAC1, we sought to test our hypothesis that SWIP-10 would influence Cu (I) homeostasis in vivo, as outlined earlier. Here, we

employed a recently developed, Cu(I)-specific fluorescent probe, Copper Fluor-4 (CF4) (37). Chun et al. previously demonstrated that CF4 staining in *C. elegans* in vivo (31), accumulates in lysosome-like intestinal granules (31), staining that colocalizes with the Cu(I) transporter CUA-1 and can be significantly reduced by the Cu(I) specific chelator bathocuproinedisulfonic acid (BCS). Staining of *swip-10* mutants with CF4 revealed significantly fewer granules with bright fluorescence vs WT animals (Fig. 2 A–C). We confirmed our image-based analyses using an objective, fluorescent plate reader-based approach. Here, CF4 intensity in *swip-10* mutants was again significantly decreased compared to WT worms (Fig. 2D).

Loss of *swip-10* Impairs Systemic Mitochondrial Respiration, ATP Production and Elevates Oxidative Stress In Vivo. The vital role played by Cu(I) in sustaining mitochondrial function and suppressing oxidative stress led us to explore whether these capacities are impacted in *swip-10* mutants. To this end, we measured basal O₂ consumption in living worms using an Oroboros Oxygraph 2 k respirometer. These studies revealed a nearly 50% reduction in O₂ consumption rate (OCR) in *swip-10* mutants compared to WT animals, consistent with a significant perturbation of mitochondrial energy production (Fig. 3A). Follow-up studies revealed significantly reduced ATP levels in *swip-10* mutants (Fig. 3B). Although a sensitive platform that

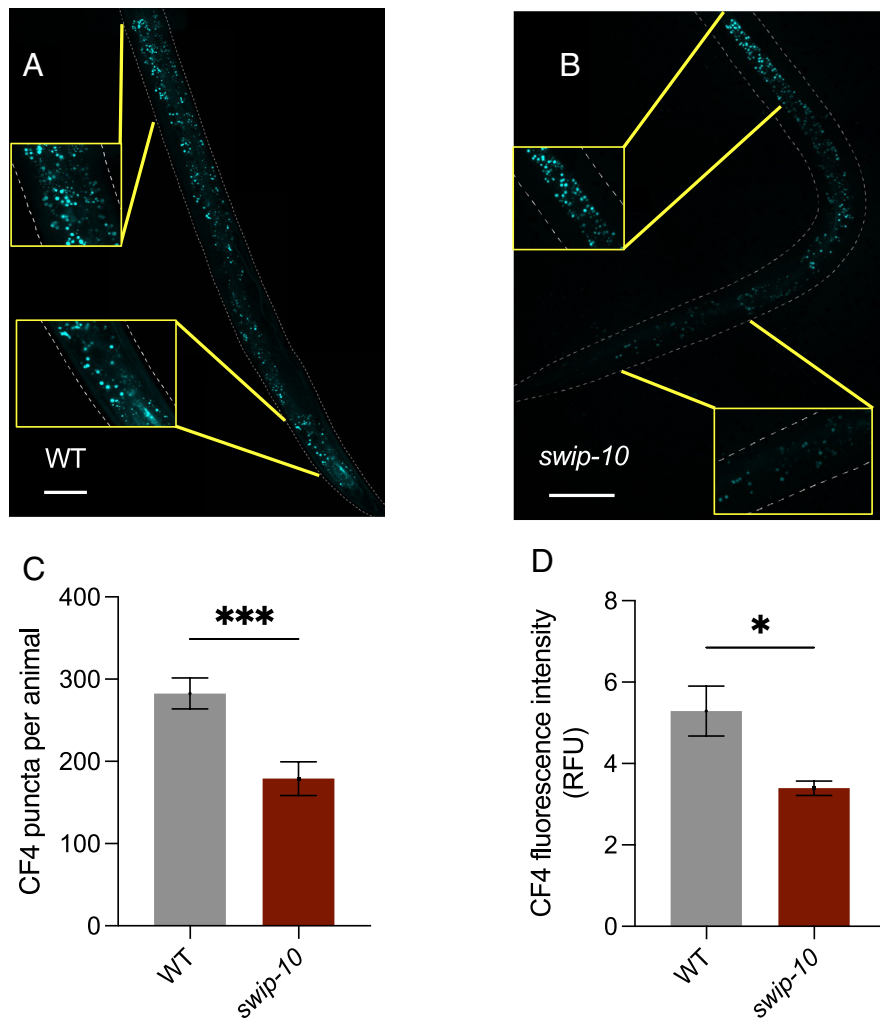


Fig. 2. Systemic Cu(I) levels are sustained by expression of *swip-10*. (A and B) Representative images of CF4 labeled worms obtained via 60 \times confocal microscopy, using excitation laser at 560 nm. Insets are higher magnification representation of CF4 puncta in comparable regions of WT and *swip-10* mutant. Scale bar is 50 microns. (C) Number of puncta were quantified using an automated analysis in Fiji (ImageJ) by setting a threshold held constant for every image where particle counts were then measured. Confocal images from 25 animals in each genotype were used as individuals for quantitation. Analysis performed from maximum projection confocal images. A total of 25 animals per condition were analyzed. Statistical analyses were performed using one-sided Student's *t* test. Puncta are found mainly in the intestinal section of the animal. Whole worm images were captured and used for analysis. (D) CF4 fluorescence intensity measured with a fluorescent plate reader (FlexStation 3, Molecular Devices) comparing WT and *swip-10*. 400 animals were added in 100 μ l to each well. Five technical replicates averaged for each biological replicate. Five biological replicates used for analysis. Statistical analyses were performed using one-sided Student's *t* test. **P* \leq 0.05. ****P* \leq 0.001.

can be used with the addition of drug compounds to inhibit or stimulate various mitochondrial complexes, the low-throughput setup of the Oroboros system limited our ability to detect changes in OCR by pathways independent of mitochondrial oxidative phosphorylation (OXPHOS) and to assess maximal capacity for mitochondrial respiration. Therefore, we assessed OCR using a Seahorse XF96 respirometer which provides a capacity to add drugs sequentially to the same sample (Fig. 3C), such as mitochondrial uncouplers and electron transport chain inhibitors (38). Here, we found a comparable and significant reduction in basal OCR in *swip-10* mutants similar to the Oroboros platform (Fig. 3D). Using the drug carbonyl cyanide-4 (trifluoromethoxy) phenylhydrazone (FCCP) to uncouple electron transport from ATP production, and thereby drive maximal OCR, we observed that where *swip-10* mutants reached a similar OCR as WT animals (Fig. 3E), indicative of a perturbation of mitochondrial function in *swip-10* mutants at or before complex IV, rather than a change in mitochondrial number or capacity. Upon addition of sodium azide to inhibit complex IV, which stops all mitochondrial oxygen consumption, WT and *swip-10* OCR dropped significantly to reveal the level of non-mitochondrial OCR capacity, which displayed no difference between WT and *swip-10* (Fig. 3F). Overall, these findings are consistent with reduced basal OCR in *swip-10* mutants as arising from diminished coupling of electron transport to ATP production.

Due to the use of Cu(I) by multiple enzymes involved in ROS elimination, including mitochondrial SODs (39–41), the

pronounced loss of mitochondrial function in *swip-10* mutants reported above, and our prior findings demonstrating elevated expression of an oxidative stress-sensitive reporter (15), we sought direct evidence for systemic oxidative stress in these animals. To accomplish this objective, we stained worms with the ROS-sensitive fluorophore 2',7'-dichlorofluorescein diacetate (DCFDA) (representative images in Fig. 4A and B). As quantified in Fig. 4C, we detected significantly elevated DCFDA fluorescence in *swip-10* mutants as compared to WT animals. Additionally, we used an HPLC approach with worm extracts to evaluate whether ROS elevations are accompanied by alterations in reduced (GSH) and/or oxidized (GSSG) forms of glutathione, as well as how these changes impact whole worm redox potential (GSSG/GSH). We found that *swip-10* mutants exhibit a significantly decreased level of GSH (Fig. 4D), a nonsignificant elevation in GSSG (Fig. 4E), and a significantly decreased redox potential (Fig. 4F) as compared to WT animals.

Cu(I) Is Both Necessary and Sufficient for the Generation of Changes in OCR, ROS, and Gene Expression Sensitive to these Alterations.

If the metabolic and neurodegenerative changes observed with *swip-10* mutants derive from altered Cu(I) homeostasis, then pharmacological manipulations that restore Cu(I) levels should rescue *swip-10* phenotypes, whereas manipulations that diminish Cu(I) in WT animals should phenocopy *swip-10* phenotypes in WT animals. Indeed, both elesclomol (ES, 5 μ M), an organic Cu(I) chaperone (42), and CuCl₂ (10 μ M), which elevates Cu(I) in the reducing environment of the cell cytoplasm

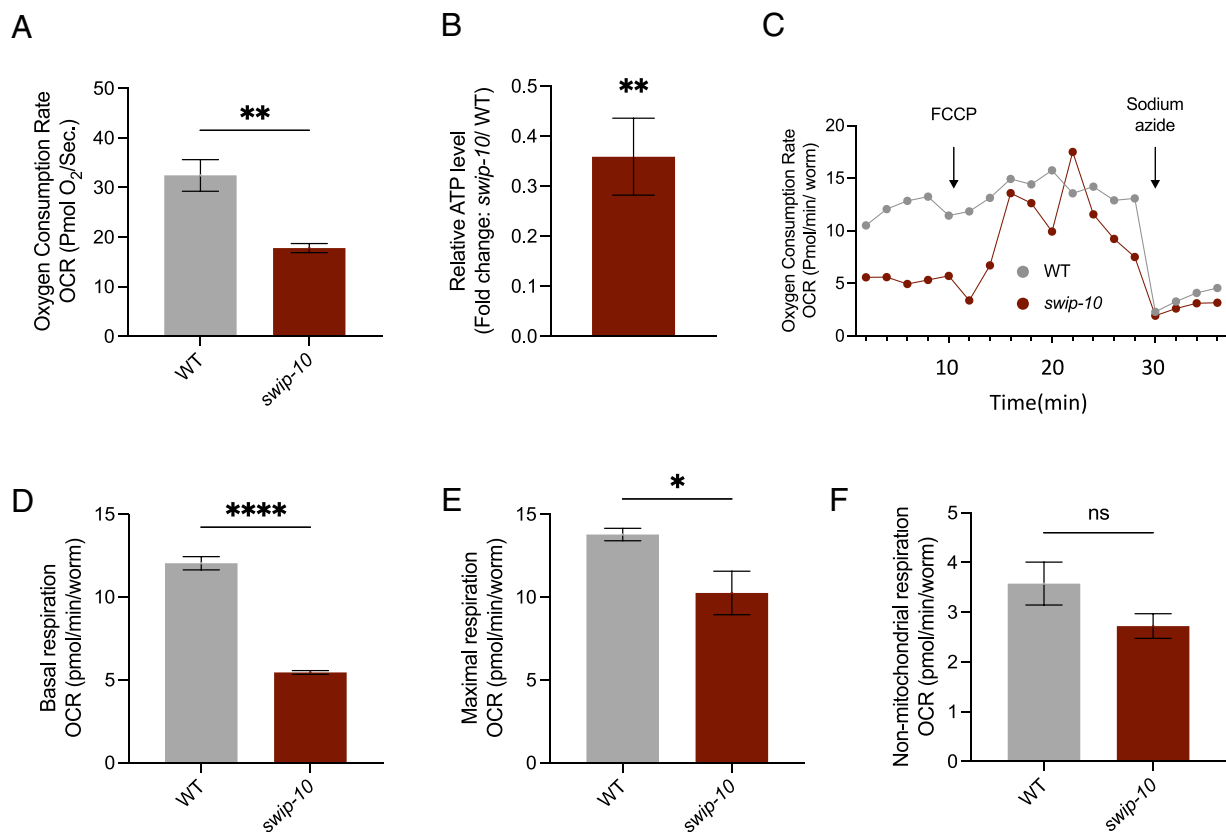


Fig. 3. *swip-10* mutation impairs mitochondrial activity. (A) Basal Oxygen consumption rate (OCR) recording from Oroboros Oxygraph 2 K. 400 animals used for each experiment. Five biological replicates used for analysis. (B) Quantification of ATP using an ATP determination kit. Data shown as average fold change of *swip-10* levels relative to N2. A one-sided Student's *t* test was used to determine significance comparing raw values (*swip-10*/N2). (C–F) OCR measured by Seahorse Respirometer, five biological replicates used for analysis. (C) Representative trace recording from Seahorse experiments. The X-axis displays each measurement period where probe is inserted into well and when the different drug compounds are added by the instrument. (D) Basal recordings from animals before the addition of any drug. (E) Maximal respiration induced by addition of FCCP (10 μ M). (F) Nonmitochondrial respiration measured after the addition of the mitochondrial inhibitor sodium azide. (A–F) All experiments noted here were performed using whole, intact worms. (A, C–F) were analyzed using one-sided Student's *t* test. **P* \leq 0.05.

(31), fully rescued the OCR and ROS phenotypes of *swip-10* mutants (Fig. 5 A and B). Rescue of OCR and ROS perturbations in *swip-10* animals was found to be paralleled by a normalization of expression of genes linked to Cu(I) availability, including the Cu(I) specific transporter, *chca-1* (*CTR1* ortholog), and the cytoplasmic Cu(I) chaperone *cuc-1* (*ATOX1* ortholog), which were both found to be elevated in *swip-10* mutants (Fig. 5C). Similarly, expression of *skn-1* (ortholog of *NRF2*), *gst-4* (ortholog of *GST*), and *sod-2* (ortholog of mitochondrial *SOD2*), genes whose expression is associated with mitochondrial dysfunction and oxidative stress, were increased in *swip-10* animals, but restored to WT levels by either ES or CuCl_2 (Fig. 5C). Conversely, treatment of WT worms with the Cu(I) chelator BCS (10 μ M) reproduced the diminished OCR and the elevated ROS of *swip-10* mutants (Fig. 5 D and E). Importantly, BCS treatment of WT animals phenocopied the DA neuron degeneration observed in *swip-10* mutants, whether assessed in aggregate (Fig. 5F) or broken out into individual components (*SI Appendix*, Fig. S5 A–C), whereas ES and CuCl_2 partially, but significantly rescued *swip-10* DA neuron degeneration (Fig. 5 F and G and *SI Appendix*, Fig. S6).

Glial Expression of *swip-10* Governs Systemic Cu(I) Production and Changes in OCR and ROS and Gene Expression. Early in development, *swip-10* is expressed broadly throughout the animal, only becoming restricted to glial cells in later larval stages. Therefore, it is possible that the reductions found in Cu(I) storage granules and the alterations seen in mitochondrial function and oxidative stress in *swip-10* mutants arise from glial-independent

mechanisms, despite glial requirements for *swip-10* in sustaining swimming behavior and suppressing DA neuron degeneration (14, 15). Therefore, we assessed support of systemic phenotypes as noted above, by reexpression of WT *swip-10* selectively in glial cells. As observed for Swip and DA neuron degeneration, driving expression of *swip-10* using a pan-glial promoter *ptr-10* revealed comparable numbers of Cu(I) containing granules as detected in WT animals (Fig. 6A). Similarly, OCR, elevated ROS, and Cu(I) associated gene expression were also normalized (Fig. 6 B–D).

Metabolome Perturbations of *swip-10* Mutants Indicate Deficits in Mitochondrial Function and Energy Homeostasis. Our ability to detect changes in OCR and measures of oxidative [and ER (15) stress in whole worms indicates that *swip-10* governs the status of multiple metabolic pathways beyond those of DA neurons. To pursue the broader consequences of this finding, we pursued a global, untargeted liquid chromatography coupled high-resolution mass spectrometry (LC-HRMS)-based approach to assess metabolite alterations in *swip-10* mutants. Seeking to maximize analyte coverage of polar and nonpolar metabolites we used both hydrophilic interaction LC (HILIC, under positive ionization) and C18 (under negative ionization) columns, respectively. We then employed a metabolome-wide analysis (MWA) approach, using multiple Welch's *t* tests, and a supervised dimensionality reduction approach, using partial least-squared discriminant analysis (PLS-DA), to assess the metabolic features driving the variation between WT and *swip-10* mutant samples. These analyses revealed nonoverlapping MS features for WT and *swip-10*

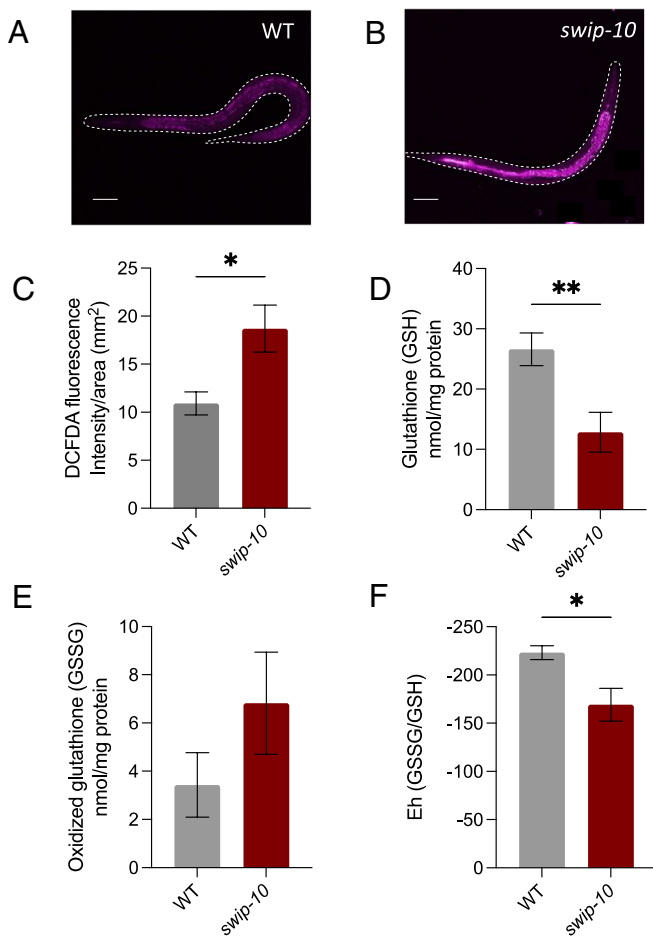


Fig. 4. Elevated oxidative stress in *swip-10* mutants. (A and B) Representative images for DCFDA staining obtained by confocal microscopy. Images captured with a 20 \times lens using an excitation laser of 488 nm. Scale bar is 50 microns. (C) Quantification of fluorescence intensity of animals treated with 50 μ M DCFDA. Intensity average normalized to total size of animal (mm²). Normalized intensity/area measurements were taken from 10 animals and averaged. Analysis was performed from the average of 5 independent measurements. Statistical analyses were performed using one sided Student's *t* test. (D–F) Targeted glutathione measurements using HPLC. (D) Total levels of reduced glutathione (GSH). (E) Total levels of oxidized glutathione (GSSG). (D and E) Statistical analyses were performed using Student's *t* test. (F) Redox potential (Eh) measured as the ratio of GSSG/GSH. Wilcoxon rank sum test performed for analysis of Eh ratio. *W* = 20. (D–F) Each independent measurement was performed using approximately 500 animals. Eight biological replicates tested. **P* \leq 0.05

mutants that can be readily resolved by PLS-DA (Fig. 7A and C). Altogether, we obtained 397 features from eluates in our HILIC positive column (Fig. 7B) and 582 features from the C18 negative column were significantly altered comparing WT and *swip-10* samples using the MWA approach (Fig. 7D).

To nominate metabolic pathways underlying the altered metabolic features found in *swip-10* mutants, we utilized the program mummichog (43) to assign putative identity to molecules based on the statistical likelihood of shared participation in biochemical networks. Virtually all of the pathways nominated can be directly linked to metabolic responses arising from, or contributing to, mitochondrial function and energy homeostasis including amino acid, fatty acid, sugar, steroid-hormone, and pyruvate linked metabolic pathways (44) (Fig. 8A and B). Conspicuously, the strongest pathway finding involves steroid biosynthesis and metabolism, processes previously found to be significantly dependent on both mitochondrial function (45) and Cu(I) homeostasis (46–48).

Discussion

Although Cu is critically important for metabolic functions of virtually every cell type, the energetically demanding cells of the brain are among the most sensitive to Cu dyshomeostasis (49). Not surprisingly, diseases that feature a disruption in Cu homeostasis, such as Wilson's and Menke's disease, feature heightened risk for neurodegenerative disease, including AD and PD (8). Despite the critical roles that require control of Cu ion homeostasis, the mechanisms that dictate the balance between Cu(I) and Cu(II) levels, particularly in the brain, remain an area of investigation. As described above, our efforts to understand how glial *swip-10* expression noncell autonomously regulates neuronal signaling and viability has led us to findings that the gene plays a prominent role in Cu(I) homeostasis and its role, broadly, in mitochondrial function and suppression of oxidative stress. Moreover, we show that glial cells, making up only approximately 5% of total cells in the worm, support this activity systemically, and when defective can lead to neurodegeneration.

The single recognizable structural domain of *swip-10*, bearing the mutations found in our genetic screen (19) offered us little insight as to the molecule's function given the variety of molecules hydrolyzed by MBDs in eukaryotic proteins (35, 50). Thus, we were excited by work deorphanizing MBLAC1, the closest mammalian SWIP-10 ortholog. This work revealed MBLAC1 to be a replication-dependent, histone pre-mRNA endonuclease. Functional studies with HEK-293 cells with diminished or absent *Mblac1* expression demonstrated alterations in cell cycle progression (27), in keeping with the well-known role played by histones in chromatin formation following DNA replication. Despite the elegance of this work, we were puzzled as to the relevance of this mechanism given the functional and neurodegenerative changes of postmitotic, glial-ensheathed neurons observed in *swip-10* mutants. The remarkable finding that H3:H4 histone complexes possess an essential Cu(II) reductase activity in yeast (9) suggested an alternative hypothesis, that *swip-10* mutants may fail to support production of Cu(I), leading to deficits in mitochondrial function, oxidative stress, and other vital processes that could explain both Swip and neurodegeneration. Our current study provides strong support for such a mechanism.

To date, we have been unable to reconstitute the enzymatic activity of SWIP-10 in mammalian cells, analogous to the Pettinati et al. studies. First, SWIP-10 possesses a long, nematode-specific N-terminal domain (14) lacking in other species, including mammals. The function of this domain has yet to be identified and it is possible that it regulates the stability or function of SWIP-10 in the absence of regulatory modifications or N-terminal cleavage as has been shown for the MBD containing protein PNKD where disease-associated mutations block cleavage, leading to rapid degradation (51). In the future, studies using the isolated MBD of SWIP-10 may be able to demonstrate RNA hydrolysis. Second, coexpression of *C. elegans* SWIP-10 associated proteins may be needed to localize SWIP-10 to the RNA template and promote hydrolytic activity. RD histone pre-mRNA, the hypothesized target of SWIP-10, are not polyadenylated, but rather possess a 3' stem loop that recruits stem loop binding protein (SLBP) and other factors, including the hydrolytic enzyme needed to cleave away sequences 3' of the stem loop, thereby promoting the nuclear export, translation, and stability of RD-histone mRNA (52). One of these complexes utilizes a *C. elegans*-specific endo-siRNA for histone RNA processing. Third, Pettinati et al. demonstrated that only a subset of histone pre-mRNAs are processed by MBLAC1, and as such a suitable *C. elegans* RD histone RNA needs to be identified to establish the assay.

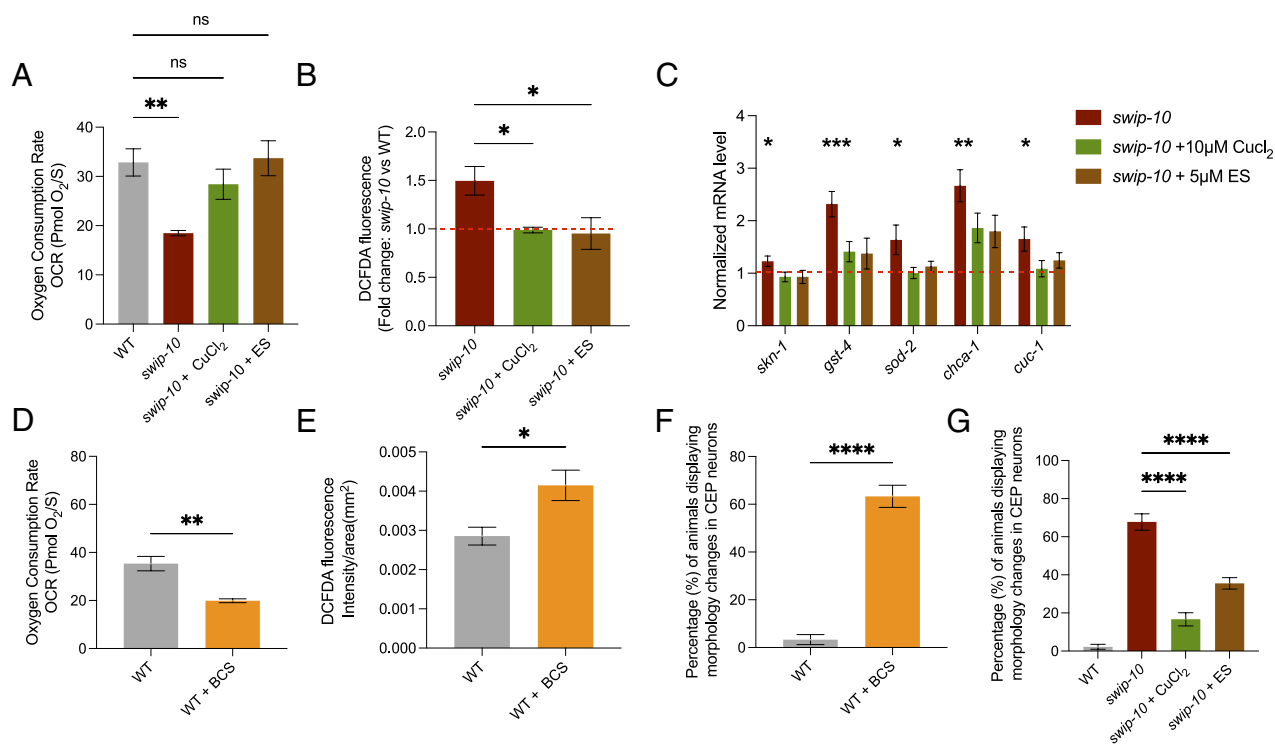


Fig. 5. Role for Cu(I) in supporting DA neurons via homeostasis of oxidative stress and mitochondrial function. (A–C) Animals either untreated or grown on agar plates containing 10 μM CuCl₂ or 5 μM elesclomol (ES). (D–F) N2 animals grown on agar plates containing 10 μM BCS until ready for experimentation. (A) Basal OCR determined by the Oroboros Oxygraph respirometer as an average of steady state recordings over 10 min. 400 animals used for recording. Ordinary one-way ANOVA used for analysis. (B) Measurements of ROS levels of animals treated with DCFDA. Confocal microscopy images obtained were used to quantify relative fluorescence intensity normalized to size of each animal. Student's *t* test used for statistical analysis. (C) Relative gene expression levels quantified via quantitative PCR. All genes normalized to the housekeeping gene actin. Two technical replicates used for each measurement. At least seven biological replicates performed for all experiments. The one-sample *t* test was used for statistical analysis. The dashed red line indicates the normalized value of 1 for fold change relative to wildtype (N2) animals. (D) Basal OCR recordings (Oroboros) as described previously. Ordinary one-way ANOVA used for statistical analysis. (E) Measurements of ROS levels of animals treated with DCFDA. Confocal microscopy images obtained were used to quantify relative fluorescence intensity normalized to size of each animal. Student's *t* test was used for statistical analysis. (F and G) Quantification of morphology characteristics of DA neurons. Total population percentage of animals displaying one or more characteristic of degeneration. (G) Animals either untreated or grown on agar plates containing 10 μM CuCl₂ or 5 μM elesclomol (ES). (F) Statistical analysis was performed by one-sided Student's *t* test. (G) Statistical analysis was performed by ordinary one-way ANOVA. **P* ≤ 0.05. ****P* ≤ 0.01. *****P* ≤ 0.0001.

If SWIP-10 processes RD histone pre-mRNA through a mechanism equivalent to that of MBLAC1, shared structural features encompassing the active sites of these enzymes should be evident. Indeed, our comparative structure studies of the MBDs of these proteins and others in the gene family provide compelling support that SWIP-10 plays an equivalent role as MBLAC1 in the worm. SWIP-10 has yet to be crystalized and as such, for comparative analyses with MBLAC1 and other gene family members for which such structures are available, we used an AlphaFold structure. Prior to initiating this effort, we validated that an AlphaFold MBLAC1 MBD model exhibits close overlap with the same sequences of the MBLAC1 crystal structure. Here, we obtained an RMSD of 0.2 Å, strongly supportive of our approach. We also obtained a sub-Å RMSD (0.5) comparing the modeled SWIP-10 MBD with the crystalized MBLAC1 MBD and obtained high (90%) overlap between the two structures with STAMP. We found good, but reduced, overlap of SWIP-10 with other family members, highest among these being other RNA processing enzymes and lowest being enzymes that target structurally distinct substrates (e.g. glutathione derivatives). Our model also demonstrates the position of a nonconservative, loss of function mutation (Gly427Asp) in SWIP-10 that lies immediately adjacent to a metal binding Asp residue predicted from MBLAC1 structure and mutagenesis to be essential for hydrolysis of histone pre-mRNA (35). Not only does the alignment of SWIP-10 with MBLAC1 exceed that seen with other members of the gene family, the orientations of side chains of conserved residues between SWIP-10 and MBLAC1 are

exceedingly well-aligned. In contrast, although the position of metal binding residues among functionally characterized members of the gene family with distinctly structured substrates are expectedly similarly positioned, the structure of the substrate binding pocket is quite different and the side chain positions of nonmetal binding residues in the other MBDs considered much less well-aligned. Together, these studies make a strong statement that the type and size of substrate and enzymatic activity of SWIP-10 and MBLAC1 are conserved, consistent with our hypothesis. Although our computational modeling of SWIP-10 supports our hypothesis that the mammalian ortholog is MBLAC1, this has not been shown experimentally. Thus, it remains possible that the alterations in Cu(I) shown in this manuscript may be indirect from affecting an unknown metabolic pathway, rather than the proposed mechanism by which SWIP-10 proposes the production of H3 histones which are then involved in the production of Cu(I). This will be further investigated by assessing RNA endonuclease assay of SWIP-10, as well as a thorough analysis of RD histone expression in *swip-10* mutants.

Our initial explorations of Cu homeostasis in *swip-10* mutants and WT animals using inductively coupled plasma MS (ICP-MS) demonstrated no significant changes (*SI Appendix*, Fig. S7). However, this approach does not distinguish Cu(I) from Cu(II) and would likely fail to detect changes in the relative ratio of these molecules since a loss of one form may elevate the other. Thus, we turned to a more selective approach, capitalizing on the Cu(I) specific fluorescent probe, CF4. CF4 had already been validated in *C. elegans*

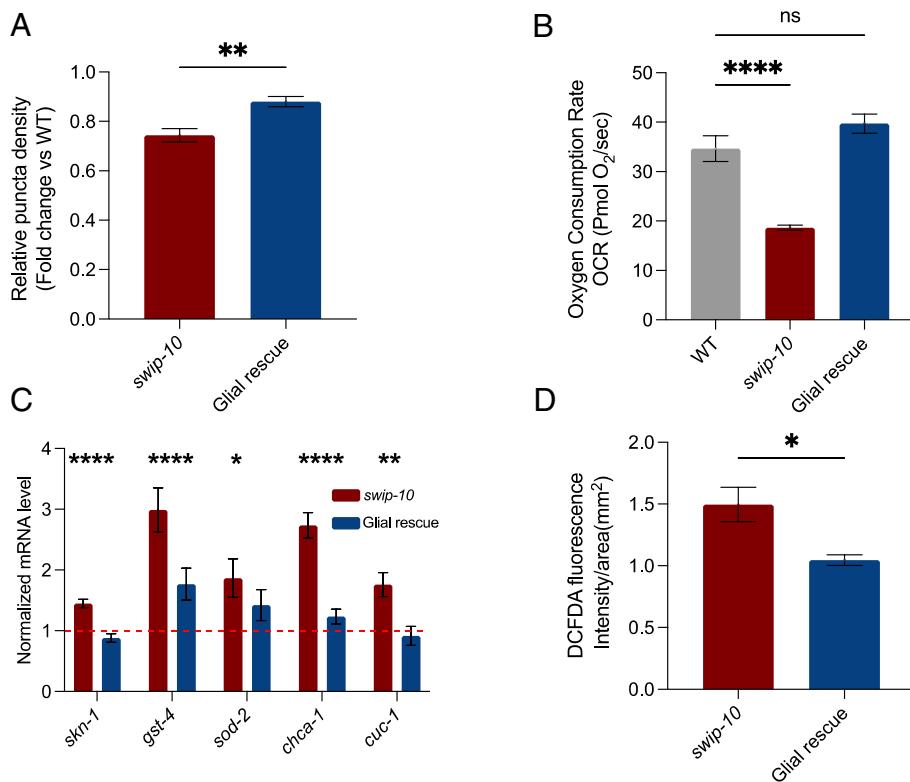


Fig. 6. Glial expression of *swip-10* dictates global Cu(I) homeostasis, oxidative stress levels, and mitochondrial function. (A) Glial rescue of attenuated Cu(I) levels throughout the entirety of the body in *swip-10* mutants. 25 animals assessed per condition. Statistical analyses were performed using one-sided Student's *t* test. (B) Basal OCR determined by the Oroboros Oxygraph respirometer as an average of steady state recordings over 10 min. 400 animals used for recording. Ordinary one-way ANOVA used for analysis. (C) Relative gene expression levels quantified via quantitative PCR. Red bars indicate changes in *swip-10* mutants, blue bars are the "glial rescue" strain. Two technical replicates used for each measurement. A minimum of six biological replicates were tested for all experiments. Data were analyzed using the one-sample *t* test. The dashed red line indicates the normalized value of 1 for fold change relative to WT (N2) animals. (D) Measurements of ROS levels of animals treated with DCFDA. Confocal microscopy images obtained were used to quantify relative fluorescence intensity normalized to size of each animal. Student's *t* test was used for statistical analysis. Glial rescue strain contains approximately 80 to 90% transgenic animals expressing *swip-10* only under the pan-glial promoter (*ptr-10*). **P* ≤ 0.05. ****P* ≤ 0.01. *****P* ≤ 0.0001.

for its ability to detect diminished Cu(I) levels arising from treatment of animals with the Cu(I) chelator BCS, as well as the loss of intestinal Cu(I) stores due to loss of the Cu(I) transporter (CUA-1) (31). Indeed, *swip-10* mutants demonstrate a loss of Cu(I) signal, whether quantified by counting the number of intestinal storage granules or by the more objective measurement of fluorescence intensity in a plate reader format (Fig. 2D). Importantly, the cross-validation of imaging and plate reader results presented here should permit future high-throughput analyses of Cu levels in *swip-10* mutants in the context of regulatory mutations or drugs. We have not pursued the nature of these granules here, but they resemble the lysosomal-type intestinal granules that serve as the major storage site in worm for Zn (53). Further studies are needed to determine whether distinct granules store Zn, Cu, and other metals, whether they may discriminate Cu(I) from Cu(II), and whether their role is to eliminate high-toxic levels of Cu or can be mobilized for systemic secretion during periods of Cu insufficiency. Importantly, these granules are far from the glial cells where rescue studies express SWIP-10 to regulate energetics and systemic metabolism. In future studies, it will be important to determine how and under what conditions glial SWIP-10 communicates with peripheral cells to regulate body-wide Cu(I) homeostasis. We envision two main possibilities. SWIP-10 expressing glial cells may act as a critical site for Cu(I) production following dietary uptake of Cu(II) which is then circulated throughout the animal to support cell metabolism and suppression of oxidative stress and neuronal health. Alternatively, glia may utilize cell autonomous, Cu(I)-dependent mechanisms to support the health and function of ensheathed neurons as well as more distant, nonneuronal cells. At this point, it is also possible that glia achieve this communication via inducing neurons they ensheath to secrete these factors. Both the direct and indirect pathways discussed here currently have precedents in *C. elegans* (24, 54). In mammals, glia, particularly astrocytes (55), have been identified as a major source of brain Cu homeostasis, with the liver primarily serving this role in the periphery. The systemic

contribution of glial SWIP-10 to whole body Cu(I) homeostasis parallels findings of an impact on systemic proteostasis by glia (24, 25), and can be linked to a prior demonstration of systemic oxidative stress in *swip-10* mutants (15). Although we have yet to evaluate Cu(II) levels *swip-10* mutants might display an increase in Cu(II) due to the lack of a significant change in total Cu, possibly contributing for some or the phenotypes documented in this study. Recently, a Cu(II) specific probe, similar to CF4, has been reported (56), affording an opportunity to explore this question directly in future studies.

Metabolic disruptions have been implicated in risk for virtually all neurodegenerative diseases (57). Neurons are particularly dependent on mitochondrial mechanisms of ATP synthesis (58) which sustains ion gradients, synaptic release of neurotransmitters and buffering Ca²⁺ that otherwise can activate apoptotic cascades (59), increasing attention to mitochondrial modulation for therapeutic potential (6). Our hypothesis predicts that *swip-10* mutants should display deficits in Cu(I)-dependent energy production, changes that would be predicted to contribute to neuronal dysfunction and possibly neurodegeneration. In this regard, basal OCR deficits in *swip-10* mutants were shown using two different methods, both yielding equivalent results with respect to basal OCR. The fact that these deficits were identified in whole worms and can be rescued by glial specific expression of WT *swip-10* confirms conclusions drawn from CF4 studies that glial *swip-10* plays a broader role than the signaling and health of glial-ensheathed neurons. The Seahorse respirometry studies we present here also demonstrate that *swip-10* mutants display a maximal OCR similar to WT as well as normal nonmitochondrial OCR, typically considered to arise from oxygenase-type enzymatic reactions. Rather, *swip-10* animals possess a significantly reduced basal OCR, with pharmacological studies indicating that the deficit arises at or before Complex IV. Notably, Complex IV or cytochrome c oxidase is a multiprotein complex that relies on Cu(I) to conduct electron transfer to oxygen, creating the electromotive force needed by Complex V for ATP synthesis. These

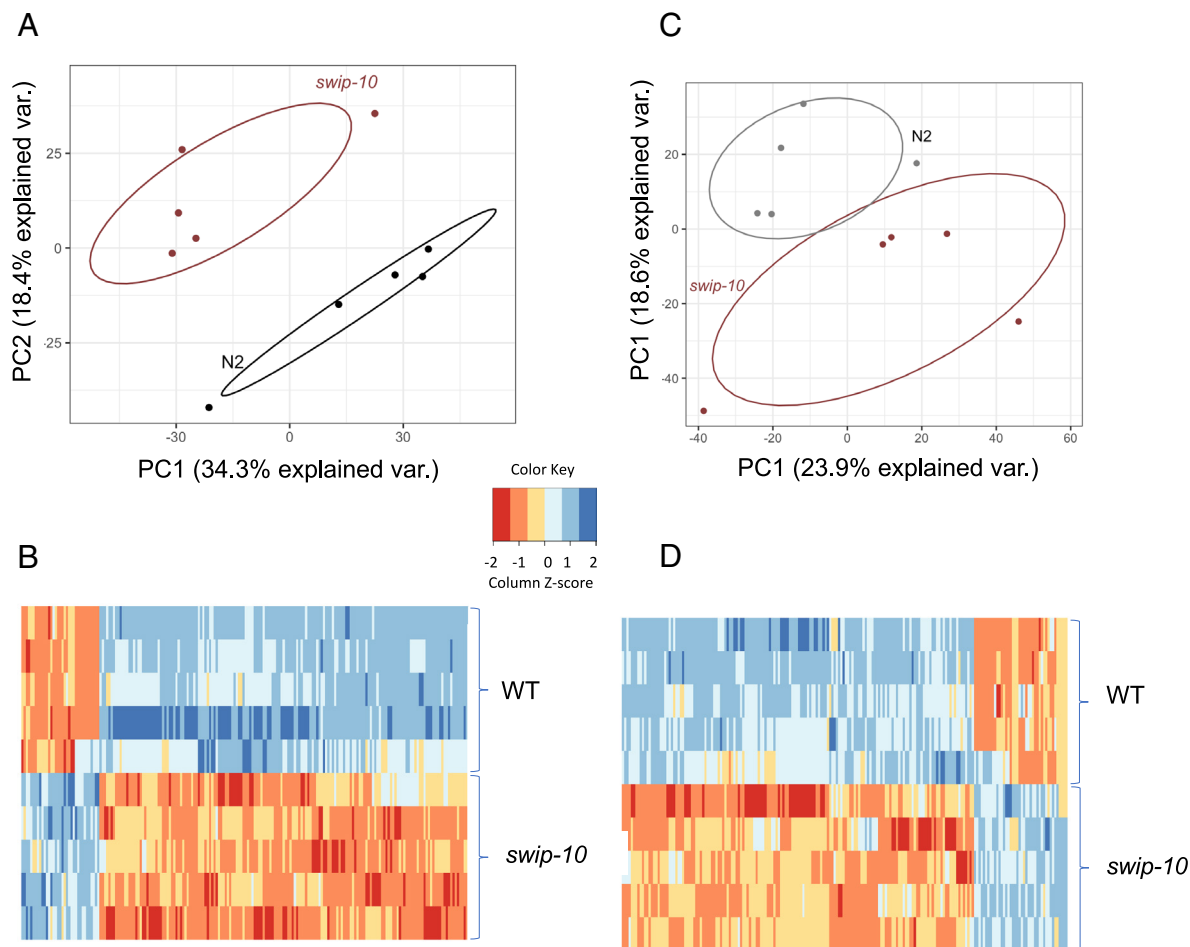


Fig. 7. Metabolomic assessment of *swip-10* mutants. Synchronized animals were grown up to the L4 stage prior to metabolite extraction and subsequent chromatography. Raw mass/charge(m/z) values were used for bioinformatic analyses to assess pathways altered between N2 and *swip-10* animals. (A and B) PLS-DA and heatmap from HILIC positive column. (C and D) PLS-DA and heatmap from C18-negative column. (A–D) Statistical analyses revealed nonoverlapping metabolomic signatures between genotypes. (B and D) Rows represent individual biological replicate samples for each genotype. Columns represent altered metabolite changes. 500 healthy, intact animals were pooled for each sample for analysis.

findings are consistent with the diminished steady-state ATP levels observed in *swip-10* mutants (Fig. 3B).

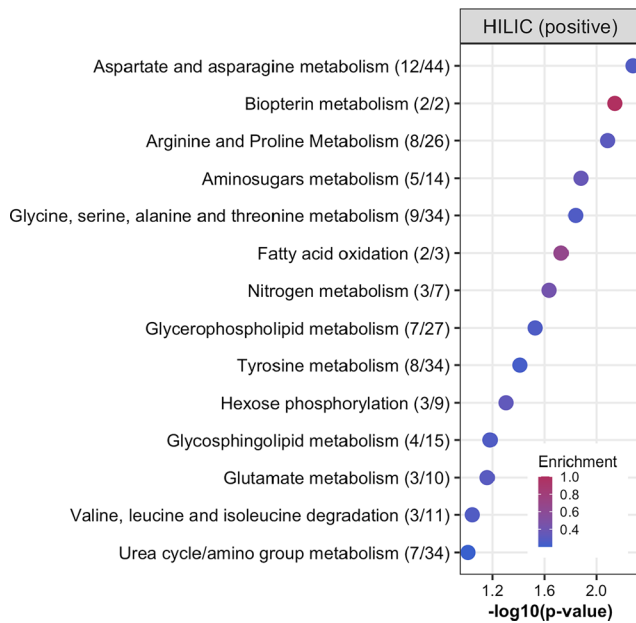
Diminished mitochondrial ATP production can lead to elevated ROS and increased cellular oxidative stress (60). Indeed, our previous *swip-10* studies displayed increased, whole body elevated expression of the ROS-sensitive reporter *gst-4::GFP* (15). Since many SODs, the major intracellular class of ROS handling proteins, are Cu(I) dependent, we pursued more direct measures of ROS in *swip-10* mutants, taking two separate approaches. First, by staining WT and *swip-10* mutants with the fluorescent ROS reporter, DCFDA, we detected a significant increase in ROS levels throughout the body of animals in vivo. As with mitochondrial function, we observed a normalization of ROS levels via glial expression of WT *swip-10*. Second, we detected diminished levels of whole-body GSH, which translates into a significant reduction in Redox Potential, indicative of a reduced capacity of cells, systemically, to eliminate ROS generated during normal metabolic reactions. Interestingly, we found elevated expression of *sod-2*, a mitochondrial SOD (Fig. 5C), though there were no changes in *sod-1*, which encodes the dominantly expressed SOD in the cytosol, supporting mitochondrial deficits as a primary driver of ROS in *swip-10* mutants.

The *C. elegans* model is highly amenable to pharmacological rescue experiments that can complement and extend genetic approaches. Capitalizing on this capacity, we assessed whether a Cu(I) deficiency is necessary and/or sufficient for the generation of

one or more of the *swip-10* phenotypes studied here. The demonstration that WT worms, grown on plates that have been supplemented with the Cu(I) chelator BCS, phenocopy the OCR, ROS, gene expression, and neurodegeneration phenotypes, of *swip-10* mutants, supports a conclusion of Cu(I) necessity. With the rescue of these *swip-10* phenotypes by culturing *swip-10* mutants on plates dosed with either CuCl_2 or ES, agents known to augment Cu(I) levels in cultured cells and animals (61), we demonstrate sufficiency of Cu(I) loss in explaining these alterations. ES, a Cu(I) chaperone, is a particularly interesting molecule can rescue Cu(I) associated deficiencies observed in a Menke's disease mouse model as well as with human carriers of disease-driving, *ATP7A* mutations (62). Based the studies reported here, consideration of elesclomol-like agents is warranted for the treatment of neurodegenerative conditions, particularly those where comorbidities, genetic markers associated with diminished *MBLAC1* expression, and/or the metabolic sequelae of *MBLAC1* reduction can be used as biomarkers to identify those most likely to benefit. Additionally, we have shown that *MBLAC1* is a target of the neuroprotective antibiotic ceftriaxone (CEF) (63). Recent development of a β -lactam (64) with properties mimicking CEF actions in rodents, but lacking antibiotic actions, will allow for the use of *C. elegans*, that grow on bacteria as a food source, for therapeutics targeting Cu(I) homeostasis through SWIP-10/*MBLAC1* pathways.

Previously, we presented evidence that the degeneration of DA neurons observed in *swip-10* mutants may be a property

A



B

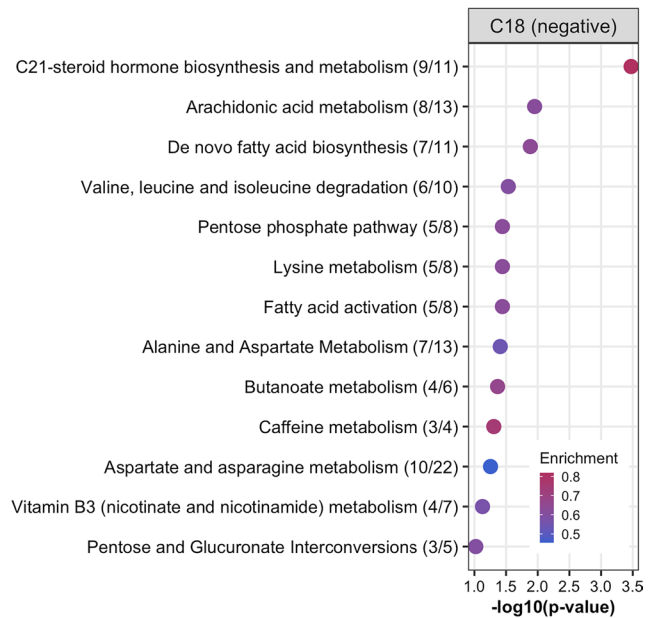


Fig. 8. Metabolic and mitochondrial networks altered by loss of *swip-10*. Mummichog 2.0 was used for pathway assessment of altered metabolites. Enrichment scores indicate abundance of known metabolites in a defined pathway. (A) Metabolites measured Hilic positive column (B) Metabolites measured from C18 negative column.

of glial ensheathment as another ensheathed neuron (OLL), known to be glutamatergic, that displays degeneration in the *swip-10* background, whereas an unsheathed neuron (BAG) shows no changes (15). Interestingly, BCS treatment induces degeneration of OLL neurons whereas BAG neurons are insensitive (SI Appendix, Fig. S4D). The basis for the Cu(I)-dependent viability of glial ensheathed neurons is currently unknown. Mammalian astrocytes are known to export Cu that is acquired by neurons for metabolic use (65), and though such a transfer cannot be assessed directly as of yet, it seems reasonable to consider this a strong possibility, particularly given the systemic phenotypes induced by head localized glial cells which may also derive from a transfer of Cu(I). Such a transfer may involve vesicle stores that fuse to release free Cu(I) or Cu(I) binding proteins analogous to mammalian ceruloplasmin (66, 67) which supports export of interorgan transfer of Cu(I) released by the liver. Interestingly, the glia surrounding degenerating neurons in *swip-10* mutants appear morphologically normal (15), suggesting that these glia make less use of the relevant Cu(I)-dependent processes whose diminished function appears to impact the viability of ensheathed neurons. Finally, Cu(I) itself need not be transferred to the neuron and be the factor whose loss produces degeneration. We have previously shown that the degeneration of DA neurons in *swip-10* mutants involves excess Glu signaling by Ca^{2+} permeant Glu receptors (15). Cu(I) has been found to inhibit NMDA-type Glu receptors (67) and, if deprived of normal levels of Cu(I), DA neuron Glu receptors may be overactivated by normal levels of Glu input. It is also possible that a glial impact of low Cu(I) levels, possibly arising from altered OCR and/or ROS production, is a reduction of Glu transporter trafficking or function that is needed to limit DA neuron excitation, and where chronic overstimulation of Ca^{2+} -dependent Glu receptors leads to neurodegeneration. Certainly, both diminished Glu clearance and reduced export of Cu(I) may occur in parallel, triggering both local and systemic changes. A general limitation of this study is the fact that we only show glial dependence of *swip-10*

mutants by glial specific expression of *swip-10* in a null mutant background. We propose a model to selectively knockout *swip-10* under a promoter that allows for temporal restriction is warranted and would help to rule out compensatory effects of a lifetime restriction of *swip-10* to glial cells. To further confirm potential systemic perturbations in Glu signaling, we used RT-qPCR to measure mRNA levels of Glu transporters involved in synaptic reuptake as well as in vesicular packaging. We found that the synaptic transporter *glt-1*, and the vesicular transporter *eat-4* to be up- and down-regulated, respectively. These results may indicate a compensatory response to excess Glu signaling by increasing reuptake of Glu via GLT1 and suppressing Glu release by decreased levels of EAT-4 (SI Appendix, Fig. S8). In this regard, we previously demonstrated that *eat-4* expression is required for Swip behavior in *swip-10* mutants (14), consistent with this idea.

Given evidence of disrupted, whole-worm mitochondrial function in *swip-10* mutants, we profiled metabolome changes in these animals to determine molecular alterations that might further inform how glial-dependent Cu(I) homeostasis impacts physiology of cells more broadly. These experiments revealed that loss of *swip-10* results in changes in pathways arising from or compensating for losses of mitochondrial metabolism. The most significant change observed in these studies was in C-21 steroid biosynthesis (Fig. 8B). Importantly, mitochondria play a crucial role in the metabolism of steroids, many of which are exported for use in downstream biochemical reactions critical for organismal metabolism (45, 68). Moreover, the biosynthesis of steroids in mitochondria impact mitochondria directly via the production of biochemical intermediates such as NADH (69). Thus, determining whether altered steroid hormone levels are a cause or a consequence of the metabolic insults seen in *swip-10* mutants justifies further investigation. We suggest that both our mouse and worm metabolomic alterations represent an impact on mitochondrial physiology. However, species differences in dietary constituents, metabolic control mechanisms, and organ systems driving the serum changes in mice and whole-body changes in

worms are major issues and thus will need further investigation to link to Cu homeostasis.

Compared to the restricted, glial expression of *swip-10*, the mammalian *MBLAC1* gene is expressed throughout the body, suggesting systemic consequences of the gene's altered expression or function. As previously noted, low expression of *MBLAC1* has been implicated in risk for AD with CVD comorbidity (26). Similar to the brain, the heart is an energetically demanding tissue, requiring a constant supply of ATP for lifelong function. Interestingly, an earlier study demonstrated that the rat *Mblac1* gene lies within a 6 Mb region that dictates blood pressure, renal function, and cardiac remodeling (70). Our own work has demonstrated an increase in heart mass in adult *Mblac1* KO mice (71). *MBLAC1* is also expressed also in the liver, the main organ supporting systemic Cu(I) homeostasis, and thus it is reasonable to expect changes in liver function as a consequence of limited *MBLAC1* expression or activity. Consistent with this idea, we identified multiple serum metabolite alterations in *Mblac1*^{-/-} mice (28) consistent with perturbed liver function, including a reduction in bile acid production (72). NADH and FADH₂ are the oxidized electron carriers supporting the mitochondrial ETC at complex I and II, respectively. The ratios of these two critical energy pathway cofactors can be used to assess the metabolic state of mitochondria (73). Using a metabolic imaging approach to measure the ratios of NADH to FADH₂ (Redox Ratio) in the liver, we found a robust decrease in the Redox Ratio in *Mblac1*^{-/-} mice, consistent with a conserved supporting a conserved mitochondrial impact of *swip-10* and *Mblac1* deficiency. Although studies connecting *Mblac1* to human are just beginning to emerge, the replicated findings of AD-CDV, paralleled by a demonstration of reduced cortical *Mblac1* gene expression justifies further effort, as does evidence that PD involves reduced mitochondrial function (74) and where genetic causes of PD have been found to interact with and/or disrupt the function of mitochondria (22, 75, 76). And demonstrate elevations in markers of oxidative stress. Our work therefore provides support for a hypothesis that metabolic changes

induced by *MBLAC1*-dependent Cu(I) homeostasis may contribute to PD risk and/or serve as a target for therapeutics in this and other neurodegenerative disorders.

Materials and Methods

All animals were grown on what OP50 bacteria and kept under standard house-keeping protocol as previously described (77). All other methods used for these studies are reported in *SI Appendix, Methods*. A table with results from the structural superimposition of SWIP-10 with group1 MBLs domains is shown in *SI Appendix, Table S1*. A table of all strains and transgenes used in this study are reported in *SI Appendix, Table S2*. Exact *P*-values for all statistical analyses are listed in *SI Appendix, Table S3*. Oligonucleotide primer sequences used for qPCR experiments are displayed in *SI Appendix, Table S4*. All individual KEGG features identified from untargeted metabolomics (summarized in Fig. 8) are available in *Dataset S1*.

Data, Materials, and Software Availability. All study data are included in the article and/or [supporting information](#). Mass spectrometry data obtained in metabolomics studies which is deposited in Zenodo (78).

ACKNOWLEDGMENTS. R.D.B. gratefully acknowledges financial support from Steven and Deborah Schmidt, Grant 22A01 from the Florida Department of Health, and a pilot award from the FAU Mangurian Center for Brain Health. V.K. and G.W.M. were supported by NIH R01 ES 023839. C.J.C. thanks NIH R01 GM 79465 for support. C.J.C. is a CIFAR fellow. We also acknowledge the generous training, advice, and/or input on the manuscript by former Blakely lab members Osama Refai, Maureen K. Hahn, and Felix P. Mayer.

Author affiliations: ^aDepartment of Biological Sciences, Charles E. Schmidt College of Science, Boca Raton, FL 33412; ^bDepartment of Environmental Health Sciences, Mailman School of Public Health, Columbia University, New York, NY 10032; ^cLaboratory of Molecular Genetics, National Institute on Deafness and Other Communication Disorders, Bethesda, MD 20892; ^dStiles-Nicholson Brain Institute, Florida Atlantic University, Jupiter, FL 33458; ^eOak Ridge Institute for Science and Education, Oak Ridge, TN 37830; ^fDepartment of Biomedical Science, Charles E. Schmidt College of Medicine, Jupiter, FL 33458; ^gDepartment of Biology, Harriet L. Wilkes Honors College, Florida Atlantic University, Jupiter, FL 33458; ^hDepartment of Chemistry, University of California, Berkeley, CA 94720; ⁱDepartment of Molecular and Cell Biology, University of California, Berkeley, CA 94720; ^jPrinceton University, Princeton, NJ 08544; and ^kDepartment of Exercise Science and Health Promotion, Charles E. Schmidt College of Science, Florida Atlantic University, Boca Raton, FL 33431

1. T. Tsang, C. I. Davis, D. C. Brady, Copper biology. *Curr. Biol.* **31**, R421–R427 (2021).
2. V. N. Pham, C. J. Chang, Metalloallostery and transition metal signaling: bioinorganic copper chemistry beyond active sites. *Angew. Chem. Int. Ed. Engl.* **62**, e202213644 (2023).
3. N. M. Garza, A. B. Swaminathan, K. P. Maremanda, M. Zulkifli, V. M. Gohil, Mitochondrial copper in human genetic disorders. *Trends Endocrinol. Metab.* **34**, 21–33 (2023).
4. V. Lalioti, G. Muruais, Y. Tsuchiya, D. Pulido, I. V. Sandoval, Molecular mechanisms of copper homeostasis. *Front. Biosci. (Landmark Ed.)* **14**, 4878–4903 (2009).
5. T. Nevitt, H. Ohrvik, D. J. Thiele, Charting the travels of copper in eukaryotes from yeast to mammals. *Biochim. Biophys. Acta* **1823**, 1580–1593 (2012).
6. Y. Wu, M. Chen, J. Jiang, Mitochondrial dysfunction in neurodegenerative diseases and drug targets via apoptotic signaling. *Mitochondrion* **49**, 35–45 (2019).
7. M. C. Linder, M. Hazeqeh-Azam, Copper biochemistry and molecular biology. *Am. J. Clin. Nutr.* **63**, 797S–811S (1996).
8. G. Gromadzka, B. Tarnacka, A. Flaga, A. Adamczyk, Copper dyshomeostasis in neurodegenerative diseases—therapeutic implications. *Int. J. Mol. Sci.* **21**, 9259 (2020).
9. N. Attar *et al.*, The histone H3–H4 tetramer is a copper reductase enzyme. *Science* **369**, 59–64 (2020).
10. O. A. Campos *et al.*, A pathogenic role for histone H3 copper reductase activity in a yeast model of Friedreich's ataxia. *Sci. Adv.* **7**, eabj9889 (2021).
11. R. Nass, D. H. Hall, D. M. Miller, R. D. Blakely, Neurotoxin-induced degeneration of dopamine neurons in *Caenorhabditis elegans*. *Proc. Natl. Acad. Sci. U.S.A.* **99**, 3264–3269 (2002).
12. P. W. McDonald *et al.*, Vigorous motor activity in *Caenorhabditis elegans* requires efficient clearance of dopamine mediated by synaptic localization of the dopamine transporter DAT-1. *J. Neurosci.* **27**, 14216–14227 (2007).
13. D. S. Matthies, P. A. Fleming, D. M. Wilkes, R. D. Blakely, The *Caenorhabditis elegans* choline transporter CHO-1 sustains acetylcholine synthesis and motor function in an activity-dependent manner. *J. Neurosci.* **26**, 6200–6212 (2006).
14. J. A. Hardaway *et al.*, Glial expression of the *Caenorhabditis elegans* gene *swip-10* supports glutamate dependent control of extrasynaptic dopamine signaling. *J. Neurosci.* **35**, 9409–9423 (2015).
15. C. L. Gibson *et al.*, Glial loss of the metallo β -lactamase domain containing protein, SWIP-10, induces age- and glutamate-signaling dependent, dopamine neuron degeneration. *PLoS Genet.* **14**, e1007269 (2018).
16. I. Mano, M. Driscoll, *Caenorhabditis elegans* glutamate transporter deletion induces AMPA-receptor/adenylyl cyclase 9-dependent excitotoxicity. *J. Neurochem.* **108**, 1373–1384 (2009).
17. O. Hornykiewicz, The discovery of dopamine deficiency in the parkinsonian brain. *J. Neural. Transm.* **70**, 9–15 (2006).
18. P. Rodriguez, R. D. Blakely, Sink or swim: Does a worm paralysis phenotype hold clues to neurodegenerative disease? *J. Cell Physiol.* **239**, e31125 (2023).
19. J. A. Hardaway *et al.*, Forward genetic analysis to identify determinants of dopamine signaling in *Caenorhabditis elegans* using swimming-induced paralysis. *G3 (Bethesda)* **2**, 961–975 (2012).
20. O. Refai, R. D. Blakely, Blockade and reversal of swimming-induced paralysis in *C. elegans* by the antipsychotic and D2-type dopamine receptor antagonist azaperone. *Neurochem. Int.* **123**, 59–68 (2019).
21. L. Iovino, M. E. Tremblay, L. Civiero, Glutamate-induced excitotoxicity in Parkinson's disease: The role of glial cells. *J. Pharmacol. Sci.* **144**, 151–164 (2020).
22. M. W. Bishop *et al.*, Hyperexcitable substantia nigra dopamine neurons in PINK1- and HtrA2/Omi-deficient mice. *J. Neurophysiol.* **104**, 3009–3020 (2010).
23. M. Katz *et al.*, Glutamate spillover in *C. elegans* triggers repetitive behavior through presynaptic activation of MGL-2/mGluR5. *Nat. Commun.* **10**, 1882 (2019).
24. R. Bar-Ziv *et al.*, Glial-derived mitochondrial signals affect neuronal proteostasis and aging. *Sci. Adv.* **9**, eadi1411 (2023).
25. A. E. Frakes *et al.*, Four glial cells regulate ER stress resistance and longevity via neuropeptide signaling in *Science* **367**, 436–440 (2020).
26. I. J. Broce *et al.*, Dissecting the genetic relationship between cardiovascular risk factors and Alzheimer's disease. *Acta Neuropathol.* **137**, 209–226 (2019).
27. I. Pettinati *et al.*, Biosynthesis of histone messenger RNA employs a specific 3' end endonuclease. *Life* **7**, e39865 (2018).
28. C. L. Gibson *et al.*, Global untargeted serum metabolomic analyses nominate metabolic pathways responsive to loss of expression of the orphan metallo β -lactamase, *MBLAC1*. *Mol. Omics* **14**, 142–155 (2018).
29. A. R. Banday *et al.*, Replication-dependent histone genes are actively transcribed in differentiating and aging retinal neurons. *Cell Cycle* **13**, 2526–2541 (2014).
30. J. Y. Hwang, K. A. Aromolaran, R. S. Zukin, The emerging field of epigenetics in neurodegeneration and neuroprotection. *Nat. Rev. Neurosci.* **18**, 347–361 (2017).

31. H. Chun *et al.*, The intestinal copper exporter CUA-1 is required for systemic copper homeostasis in *Caenorhabditis elegans*. *J. Biol. Chem.* **292**, 1–14 (2017).
32. I. Pettinati, J. Brem, M. A. McDonough, C. J. Schofield, Crystal structure of human persulfide dioxygenase: Structural basis of ethylmalonic encephalopathy. *Hum. Mol. Genet.* **24**, 2458–2469 (2015).
33. J. Jumper *et al.*, Highly accurate protein structure prediction with AlphaFold. *Nature* **596**, 583–589 (2021).
34. R. B. Russell, G. J. Barton, Multiple protein sequence alignment from tertiary structure comparison: Assignment of global and residue confidence levels. *Proteins* **14**, 309–323 (1992).
35. I. Pettinati, J. Brem, S. Y. Lee, P. J. McHugh, C. J. Schofield, The chemical biology of human metallo- β -lactamase fold proteins. *Trends Biochem. Sci.* **41**, 338–355 (2016).
36. M. Varadi *et al.*, AlphaFold protein structure database in 2024: Providing structure coverage for over 214 million protein sequences. *Nucleic Acids Res.* **52**, D368–D375 (2024).
37. T. Xiao *et al.*, Copper regulates rest-activity cycles through the locus coeruleus-norepinephrine system. *Nat. Chem. Biol.* **14**, 655–663 (2018).
38. M. Koopman *et al.*, A screening-based platform for the assessment of cellular respiration in *Caenorhabditis elegans*. *Nat. Protoc.* **11**, 1798–1816 (2016).
39. E. D. Harris, Copper as a cofactor and regulator of copper, zinc superoxide dismutase. *J. Nutr.* **122**, 636–640 (1992).
40. L. M. Ruiz, A. Libedinsky, A. A. Elorza, Role of copper on mitochondrial function and metabolism. *Front. Mol. Biosci.* **8**, 711227 (2021).
41. C. Y. Chung *et al.*, Activity-based ratiometric FRET probe reveals oncogene-driven changes in labile copper pools induced by altered glutathione metabolism. *Proc. Natl. Acad. Sci. U.S.A.* **116**, 18285–18294 (2019).
42. V. M. Gohil, Repurposing elesclomol, an investigational drug for the treatment of copper metabolism disorders. *Expert. Opin. Investig. Drugs* **30**, 1–4 (2021).
43. J. Chong, M. Yamamoto, J. Xia, MetaboAnalystR 2.0: From raw spectra to biological insights. *Metabolites* **9**, 57 (2019).
44. A. Judge, M. S. Dodd, Metabolism. *Essays Biochem.* **64**, 607–647 (2020).
45. P. Melchinger, B. M. Garcia, Mitochondria are midfield players in steroid synthesis. *Int. J. Biochem. Cell Biol.* **160**, 106431 (2023).
46. M. Colombani-Vidal, A. Barnea, Effects of castration and maturational age of male rats on the process of copper-stimulated release of luteinizing hormone releasing hormone from median eminence explants: Evidence that androgens increase the affinity of the copper-interactive sites for copper. *Neuroendocrinology* **41**, 454–461 (1985).
47. C. S. Chang, J. B. Choi, H. J. Kim, S. B. Park, Correlation between serum testosterone level and concentrations of copper and zinc in hair tissue. *Biol. Trace Elem. Res.* **144**, 264–271 (2011).
48. K. Y. Lei, Dietary copper: Cholesterol and lipoprotein metabolism. *Annu. Rev. Nutr.* **11**, 265–283 (1991).
49. S. Borchard *et al.*, The exceptional sensitivity of brain mitochondria to copper. *Toxicol. In Vitro* **51**, 11–22 (2018).
50. S. M. Diene *et al.*, Origin, diversity, and multiple roles of enzymes with metallo- β -lactamase fold from different organisms. *Cells* **12** (2023).
51. Y. Shen *et al.*, Mutations in PNKD causing paroxysmal dyskinesia alters protein cleavage and stability. *Hum. Mol. Genet.* **20**, 2322–2332 (2011).
52. W. F. Marzluff, K. P. Koreski, Birth and death of histone mRNAs. *Trends Genet.* **33**, 745–759 (2017).
53. H. C. Roh, S. Collier, J. Guthrie, J. D. Robertson, K. Kornfeld, Lysosome-related organelles in intestinal cells are a zinc storage site in *C. elegans*. *Cell Metab.* **15**, 88–99 (2012).
54. H. K. Gildea *et al.*, Glia of *C. elegans* coordinate a protective organismal heat shock response independent of the neuronal thermosensory circuit. *Sci. Adv.* **8**, eabq3970 (2022).
55. R. Dringen, I. F. Scheiber, J. F. Mercer, Copper metabolism of astrocytes. *Front. Aging Neurosci.* **5**, 9 (2013).
56. A. T. Pezacki *et al.*, Oxidation state-specific fluorescent copper sensors reveal oncogene-driven redox changes that regulate labile copper(II) pools. *Proc. Natl. Acad. Sci. U.S.A.* **119**, e2202736119 (2022).
57. V. R. Muddapu, S. A. P. Dharshini, V. S. Chakravarthy, M. M. Gromiha, Neurodegenerative diseases—Is metabolic deficiency the root cause? *Front. Neurosci.* **14**, 213 (2020).
58. G. Yellen, Fueling thought: Management of glycolysis and oxidative phosphorylation in neuronal metabolism. *J. Cell Biol.* **217**, 2235–2246 (2018).
59. M. A. Perez-Pinzon, R. A. Stetler, G. Fiskum, Novel mitochondrial targets for neuroprotection. *J. Cereb. Blood Flow Metab.* **32**, 1362–1376 (2012).
60. B. L. Tang, Glucose, glycolysis, and neurodegenerative diseases. *J. Cell Physiol.* **235**, 7653–7662 (2020).
61. S. Soma *et al.*, Elesclomol restores mitochondrial function in genetic models of copper deficiency. *Proc. Natl. Acad. Sci. U.S.A.* **115**, 8161–8166 (2018).
62. L. M. Guthrie *et al.*, Elesclomol alleviates Menkes pathology and mortality by escorting Cu to cuproenzymes in mice. *Science* **368**, 620–625 (2020).
63. C. L. Retzlaff *et al.*, Metallo- β -lactamase domain-containing protein 1 (MBLAC1) is a specific, high-affinity target for the glutamate transporter inducer ceftriaxone. *ACS Chem. Neurosci.* **8**, 2132–2138 (2017).
64. L. A. Knackstedt *et al.*, MC-100093, a Novel. *J. Pharmacol. Exp. Ther.* **378**, 51–59 (2021).
65. A. Bhattacharjee, S. Ghosh, A. Chatterji, K. Chakraborty, Neuron-glia: Understanding cellular copper homeostasis, its cross-talk and their contribution towards neurodegenerative diseases. *Metallomics* **12**, 1897–1911 (2020).
66. M. A. Cater, S. La Fontaine, K. Shield, Y. Deal, J. F. Mercer, ATP7B mediates vesicular sequestration of copper: Insight into biliary copper excretion. *Gastroenterology* **130**, 493–506 (2006).
67. R. Squitti *et al.*, Meta-analysis of serum non-ceruloplasmin copper in Alzheimer's disease. *J. Alzheimers Dis.* **38**, 809–822 (2014).
68. W. L. Miller, Steroid hormone synthesis in mitochondria. *Mol. Cell Endocrinol.* **379**, 62–73 (2013).
69. P. Gaignard *et al.*, Role of sex hormones on brain mitochondrial function, with special reference to aging and neurodegenerative diseases. *Front. Aging Neurosci.* **9**, 406 (2017).
70. M. J. Flister *et al.*, Identification of hypertension susceptibility loci on rat chromosome 12. *Hypertension* **60**, 942–948 (2012).
71. B. Ceyhan *et al.*, Optical imaging reveals liver metabolic perturbations in Mblac1 knockout mice. *Ann. Int. Conf. IEEE Eng. Med. Biol. Soc.* **2023**, 1–4 (2023).
72. J. Y. L. Chiang, J. M. Ferrell, Bile acid metabolism in liver pathobiology. *Gene Expr* **18**, 71–87 (2018).
73. D. Spejber, Being right on Q: Shaping eukaryotic evolution. *Biochem. J.* **473**, 4103–4127 (2016).
74. A. Bose, M. F. Beal, Mitochondrial dysfunction in Parkinson's disease. *J. Neurochem.* **139**, 216–231 (2016).
75. A. Kolicheski *et al.*, Early-onset Parkinson's disease: Creating the right environment for a genetic disorder. *J. Parkinsons Dis.* **12**, 2353–2367 (2022).
76. L. L. Kilarski *et al.*, Systematic review and UK-based study of PARK2 (parkin), PINK1, PARK7 (DJ-1) and LRRK2 in early-onset Parkinson's disease. *Mov. Disord.* **27**, 1522–1529 (2012).
77. S. Brenner, The genetics of *Caenorhabditis elegans*. *Genetics* **77**, 71–94 (1974).
78. V. Kalia, P. Rodriguez, R. Blakely, G. Miller, Metabolomics data associated with "Glia swip-10 controls systemic mitochondrial function, oxidative stress, and neuronal viability via copper ion homeostasis". Zenodo. <https://zenodo.org/records/13380130>. Deposited 27 August 2024.